Assessing the Ducting Phenomenon and its Potential Impact on GNSS Radio Occultation Refractivity Retrievals over the Northeast Pacific Ocean using Radiosondes and Global Reanalysis

Thomas E. Winning Jr.[1], Feiqin Xie[1] and Kevin J. Nelson[1,a]

[1] Texas A&M University – Corpus Christi, Corpus Christi, 78412, USA

[a] now at: Jet Propulsion Laboratory, California Institute of Technology, Pasadena, 91109, USA

Correspondence to: Thomas E. Winning Jr. (twinning@islander.tamucc.edu)

Abstract. In this study, high-resolution radiosondes from the MAGIC field campaign and ERA5 global reanalysis data are used to assess characteristics of the elevated ducting layer ~~characteristics~~ along ~~the~~a transect over the northeastern Pacific Ocean from Los Angeles, California to Honolulu, Hawaii. The planetary boundary layer (PBL) height (PBLH) increases as the strength of the refractivity gradient decreases westward along the transect. The thickness of the prevailing ducting layer remains remarkably consistent (~110 m) in the radiosonde data. On the other hand, the ERA5 reanalysis generally resolves the ducting features well, but underestimates the ducting height and strength, especially over the trade cumulus region near Hawaii. A simple two-step end-to-end simulation is used to evaluate the impact of the elevated ducting layer on RO refractivity retrievals. A systematic negative refractivity bias (*N*-bias) below the ducting layer is observed throughout the transect, peaking (−5.42%) ~~approximately 80 meters~~slightly below the PBLH, and gradually decreasing towards the surface (−0.5%). The *N*-bias shows strong positive correlation with the ducting strength. The ERA5 data underestimate the *N*-bias with the magnitude of the underestimation increasing westward along the transect.

1 Introduction

The troposphere, where most weather occurs, consists of two main layers: the planetary boundary layer (PBL) and the free atmosphere (FA) (Garratt, 1994). The PBL characteristics change frequently on both spatial and temporal scales and the PBL height (PBLH) can impact the exchange of heat, momentum, and particulate matter with the FA, making it a critical factor in global energy balances and water cycling (Stull 1988; Ramanathan et al. 1989; Klein and Hartmann 1993). Regular PBL observations are mainly limited to in-situ measurements from surface stations and radiosondes. However, spatially and temporally dense in-situ PBL observations are typically only available from field campaigns such as the Boundary Layer Experiment 1996 (BLX96, Stull et al. 1997), the Variability of the American Monsoon Systems (VAMOS) Ocean-Cloud-Atmosphere-Land Study Regional Experiment (VOCALS-REx, Wood et al. 2011), and the Marine Atmospheric Radiation Measurement (ARM) Global Energy and Water Experiment (GEWEX) Cloud System Studies (GCSS) Pacific Cross Section Intercomparison (GPCI) Investigation of Clouds (MAGIC, Zhou et al. 2015). Satellite observations of the PBL are also limited due to signal attenuation of the conventional infrared sounder in the lower troposphere and the low vertical resolution of microwave sounding instruments. Additionally, while the depth of the PBLH can vary from a couple hundred meters to a few kilometers (Ao et al. 2012; von Engeln and Teixeira 2013), the transition layer from the PBL to the FA is typically on the order of tens to hundreds of meters thick (Maddy and Barnet 2008), rendering ~~ineffective~~ PBL sensing from the low vertical resolution passive infrared and microwave sounders ineffective.

On the other hand, Global Navigation Satellite System (GNSS) radio occultation (RO) provides global atmospheric soundings with a vertical resolution of approximately 100 m in the lower troposphere under all weather conditions (Kursinski et al., 1997, 2000; Gorbunov et al., 2004). ~~One~~Some of the recent major GNSS RO missions ~~is~~are the Formosat-3/Constellation Observing System for Meteorology, Ionosphere, and Climate (COSMIC), later referred to as COSMIC-1 (Anthes et al. 2008), and its follow-on mission COSMIC-2 (Schreiner et al. 2020). Numerous studies have documented the high value of GNSS RO for profiling the PBL and determining the PBLH (Ao et al. 2008; Xie et al. 2008; Basha and Ratnam 2009; Guo et al. 2011; Ao et al. 2012; Ho et al. 2015; Winning et al. 2017; Nelson et al. 2021).

The advancement of the GNSS RO technique with open-loop tracking (Ao et al., 2003; Beyerle et al., 2003; Sokolovskiy et al., 2006) along with the implementation of radio-holographic retrieval algorithms (Gorbunov, 2002; Jensen et al., 2003; Jensen et al., 2004) have led to much improved PBL sounding quality. However, probing the marine PBL remains challenging, as systematic negative biases are frequently seen in RO refractivity retrievals (Xie et al. 2010; Feng et al. 2020). One major cause of ~~the~~ refractivity bias (hereafter N-bias) is the RO retrieval error due to elevated atmospheric ducting often seen near the PBLH (Sokolovskiy 2003; Ao et al. 2003; Xie et al., 2006; Ao et al., 2007). This elevated ducting ~~prevails~~is found primarily over the subtropical eastern oceans (von Englen et al., 2003; Lopez, 2009; Feng et al., 2020), and the horizontal extent of ducting in these regions can be on the order of thousands of kilometers (Xie et al. 2010; Winning et al. 2017). In the presence of ducting, the vertical refractivity gradient exceeds the critical refraction threshold for L-band frequencies (i.e., $dN/dz \leq -157$ N-units km^{-1}). The steep negative refractivity gradient is often observed in the vicinity of the PBLH, which is typically caused by an atmospheric temperature inversion, a sharp decrease in moisture, or a combination of both. When ducting is present, the Abel inversion (e.g., Fjeldbo et al., 1971) in the standard RO retrieval process encounters a non-unique inversion problem due to a singularity in the bending angle, resulting in large, systematic underestimation of refractivity (N) below the ducting layer (Ao et al., 2003; Sokolovskiy, 2003; Xie et al. 2006). The large uncertainty in RO refractivity coupled with the singularity in bending angle hinders assimilation of RO observations into numerical weather models, resulting in ~~discarding~~the rejection of a significant percentage of RO measurements inside the PBL (Healy, 2001).

To comprehensively assess the potential impact of ducting on GNSS RO retrievals, we begin by constructing a detailed ground truth of PBL ducting statistics. This is derived from an extensive set of high-resolution radiosonde data over the northeastern Pacific Ocean, a region known for prevailing ducting conditions. Subsequently, we conduct a simulation study using the radiosonde data to evaluate the N-biases caused by varying ducting characteristics. Section 2 provides details of the two data sets used for this study: high-resolution radiosondes over the northeastern Pacific Ocean and the colocated ECMWF Reanalysis version 5 (ERA5, Hersbach et al. 2020) profiles. Additionally, we discuss the colocation criteria and the detection method for ducting layer and the corresponding PBLH. Section 3 presents the ducting statistics for key variables, such as ducting height, PBLH, minimum refractivity gradient, and sharpness parameter. The characteristics of

3

91 ducting including the thickness and strength along the cross-section are also shown. Furthermore,

92 we evaluate the ducting-induced *N*-bias in GNSS RO refractivity retrievals by carrying out a two-

93 step end-to-end simulation. Section 4 summarizes the findings and discusses the direction of future

94 research.

2   Data and methods

2.1 MAGIC radiosonde and colocated ERA5 data

97 A collection of high-resolution radiosondes from the Marine Atmospheric Radiation Measurement

98 (ARM) GCSS Pacific Cross Section Intercomparison (GPCI) Investigation of Clouds (MAGIC)

99 are utilized as the primary data set in this analysis (Zhou et al. 2015; Lewis 2016). The MAGIC

100 field campaign took place from 26 September 2012 to 2 October 2013 as part of the U.S

101 Department of Energy ARM Program Mobile Facility 2 (AMF2) aboard the Horizon Lines

102 container ship, *Spirit*, which completed 20 round trip passes between Los Angeles, California and

103 Honolulu, Hawaii during the yearlong data collection period (Painemal et al., 2015; Zhou, 2015).

104 During each transit, radiosondes were launched at 6-hour intervals from the beginning of the

105 program through the end of June 2013; the observation frequency increased to every 3 hours from

106 July 2013 through the end of the campaign (Zhou et al., 2015). A total of 583 MAGIC radiosonde

107 profiles were collected during the field campaign (Zhou et al., 2015), all with a vertical sampling

108 frequency of 0.5 Hz (2 seconds), which provides an average vertical resolution of ~8 m below 3

109 km, but varies due to local vertical motion.

110 Use of this data set serves multiple benefits. First, the northeast Pacific transitions from a shallow

111 stratocumulus-topped PBL to a ~~higher~~deeper, trade-cumulus boundary layer regime along the

112 GPCI transect shown in Figure 1 (Garratt, 1994). Second, the large number of observations over a

113 12-month time frame provides high temporal (diurnal- and seasonal-scale) and spatial profiling of

114 the PBL along the GPCI transect ~~seen in~~ (Fig._1~~.~~). Finally, ducting is prevalent throughout the

115 domain over which the observations were captured creating an opportunity to perform an analysis

116 over a natural cross-section of X (zonal) and Z (vertical) dimensions.
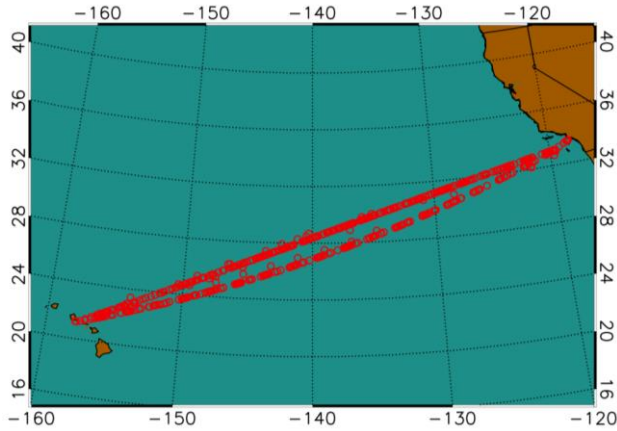
Figure 1: Location of radiosonde observations from the MAGIC field campaign October 2012–September 2013.

The radiosonde profiles are colocated with ERA5 model profiles. for this analysis. The ERA5 data have a horizontal ~~grid~~ resolution of 0.25˚x0.25˚, ~~1-hour temporal resolution, and~~ 137 non-~~linear~~equidistant vertical model levels from the surface to 0.01 hPa, and 1-hour temporal resolution. The model level density decreases with height: on average, there are 19 model levels below 1 km (10 –100 m resolution), which reduces to 8 levels between 1 and 2 km (100 – 160 m resolution), and further reduces to 5 levels between 2 and 3 km (160-200 m resolution). Each MAGIC radiosonde profile was colocated with the nearest ERA5 grid point that is within 1.5 hours of the closest 3-hourly model profile.

2.2 PBLH detection with the minimum gradient method

At GNSS L-band frequencies, the atmospheric refractivity (N in N-units) is derived from the refractive index n, where $N = (n − 1)$ x 10^6 and, in the neutral atmosphere (Kursinski et al., 1997), is a function of the atmospheric pressure (P in mb), temperature (T in K), and partial pressure of water vapor (P_w in mb) as seen in Eq. (1) from Smith and Weintraub (1953).

$$N = 77.6\frac{P}{T} + 3.73 \times 10^5 \frac{P_w}{T^2}, \tag{1}$$

Over the subtropical eastern oceans, a sharp decrease in moisture is often associated with a strong temperature inversion marking a clear transition from the PBL to the FA. ~~Both the~~The distinct decrease in moisture and the temperature inversion ~~lead~~leads to a sharp negative refractivity gradient which can be precisely detected from GNSS RO. Numerous studies have implemented

5

138   the simple gradient method to detect the PBLH, i.e., the height of the minimum refractivity
139   gradient (Xie et al., 2006; Seidel et al., 2010; Ao et al., 2012). To assess the robustness of the
140   PBLH detection with the gradient method, Ao et al. (2012) introduced the sharpness parameter
141   ($\widetilde{N}'$) to measure the relative magnitude of the minimum gradient, which is defined as the ratio of
142   the minimum vertical refractivity gradient (N'_{min}) to the root mean square (N'_{RMS}) of the refractivity
143   gradient profile from surface to 5 km as follows.

144
$$\widetilde{N}' \equiv -\frac{N'_{min}}{N'_{RMS}}, \tag{2}$$

145   In this study, the MAGIC radiosonde refractivity profiles were first interpolated to a uniform 10
146   m vertical grid and then smoothed by a 100 m boxcar window to reduce the noise in the gradient
147   profile resulting from the high sampling rate. Moreover, the 100 m smoothed radiosonde will be
148   more consistent with the vertical resolution of GNSS RO measurements (e.g.., Gorbunov et al.,
149   2004). Colocated ERA5 data were also vertically interpolated to the same 10 m grid but not
150   smoothed as these data do not contain the inherent noise as the radiosonde observations. In the
151   case of both data sets, quadratic interpolation is used to translate the refractivity profiles from their
152   native height values to a uniform height. Finally, as the elevated ducting layer is the focus of this
153   study, the lowest 0.3 km above mean-sea-level of the N-profile are excluded (e.g., Xie et al., 2012).
154   Subsequently, the height of the minimum refractivity gradient (within 0.3 km and 5 km) will be
155   identified as the PBLH.

156   **2.3 Ducting layers**

157   The refractivity gradient profile is calculated by differentiating the 10 m interpolated refractivity
158   profile with respect to height. When the vertical refractivity gradient is less than the critical
159   refraction threshold for radio waves ($dN/dz < -157.0$ N-units km^{-1}), ducting occurs (Sokolovskiy,
160   2003). A ducting layer is identified as any interval of continuous points with a vertical refractivity
161   gradient equal to or less than =157 N units km^{-1}.the critical refraction threshold. Instances of
162   multiple ducting layers occurring within a profile are present for both the MAGIC (31.5%) and
163   ERA5 (6.7%) data sets. In this study, we only recognize one dominant "ducting layer" in each
164   profile where the minimum vertical gradient is located. The ducting layer thickness (Δh) is defined
165   as the interval between the top and bottom of the ducting layer where the refractivity gradients
166   reach critical refraction. Similarly, the strength of each ducting layer (ΔN) is defined as the

167 refractivity difference between the bottom and top of the ducting layer. The ducting layer height

168 is defined as the height of the top of the ducting layer (Ao, 2007), which is generally slightly above

169 the PBLH.

170 Figure 2 shows vertical profiles of refractivity (Nda$N$-units/10), temperature (T in ˚C), and specific

171 humidity (q in g/kg) along with their respective vertical gradients (dN/dz, dT/dz, and dq/dz) from

172 a representative MAGIC radiosonde (Fig. 2a,b) case located at (23.69˚, −150.02˚), and its

173 colocated ERA5 (Fig. 2c,d) profile at (23.75˚, −150.00˚). The PBLH of the radiosonde (2.10 km)

174 is almost identical to the colocated ERA5 (2.14 km) and the "dominant" ducting layer near the

175 PBLH demonstrates similar thickness. However, a second, weaker ducting layer seen in the

176 radiosonde above the PBLH was not captured by the ERA5. ~~Note~~It should be noted that the weak

177 "saw tooth-like" gradients seen above the minimum in the ERA5 refractivity gradient (Fig. 2d) are

178 a result of the vertical derivative being calculated from the interpolated ERA5 refractivity profile

179 ~~and do not appear for larger interpolation intervals suggesting that the non-linearity of the ERA5~~

180 ~~vertical grid at this height affects the vertical gradient. These features of approximately 15 N-units~~

181 ~~km⁻¹ magnitude are only noticed in the plotting and do not impact the results of the study, as only~~

182 ~~the moisture-induced minimum gradient values are large enough in magnitude to exceed the~~

183 ~~minimum gradient threshold.~~. When interpolating the relatively coarse vertical resolution ERA5

184 ~~profile (up to 200 m in the lowest 3 km) into 10 m vertical sampling,~~the higher-order interpolation

185 could lead to fine structure in the first order derivative. However, these minor gradients do not

186 affect the estimates of minimum gradient and associated heights.

187
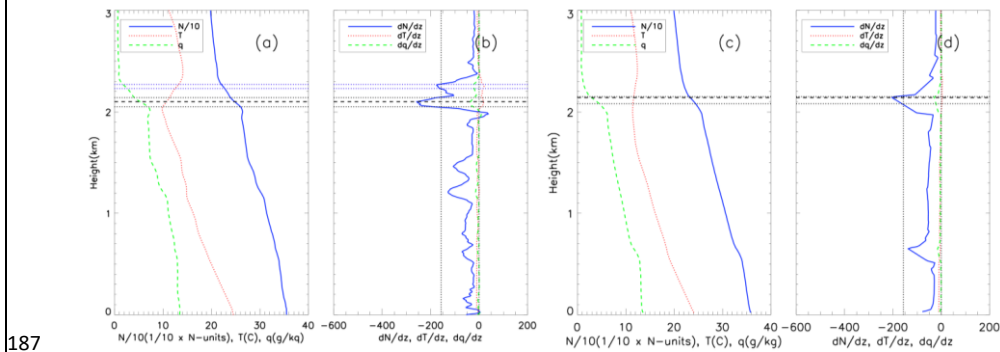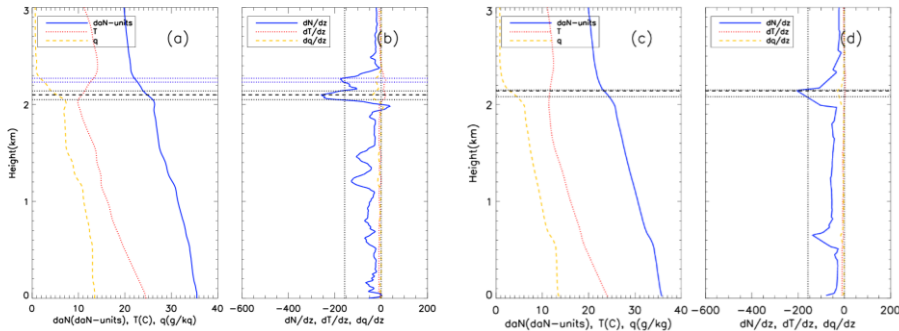
Figure 2: Vertical profiles of refractivity (~~N~~daN-units ~~/10~~, solid blue), temperature (*T* in ˚C, dotted red) and specific humidity (*q* in g kg⁻¹, dashed ~~green~~gold) for (a) radiosonde at (23.69˚, -150.02˚) launched at ~~2012~~2013-10-02, 05:30 UTC, and (c) colocated ERA5 at (23.75˚, -150.00˚); and associated gradient profiles for radiosonde (b) and ERA5 (d). The horizontal dashed line highlights the height of the minimum gradient, i.e., PBLH. The paired horizontal dotted lines represent the bottom and top of ~~the two~~any ducting layers ~~in the radiosonde profile (a and b) but only one in the ERA5 profile (c and d). .

2.4 Evaluation of GNSS RO *N*-bias resulting from ducting

In order to estimate the systematic negative *N*-bias in GNSS RO observations in the presence of ducting, we use an end-to-end simulation on the radiosonde and ERA5 refractivity profiles. The simulation consists of a two-step process adapted from Xie et al. (2006). The first step is to simulate the 1-dimensional GNSS RO bending angle as a function of impact parameter (i.e., the product of refractive index and the radius of the Earth's curvature) by forward Abel integration of an input refractivity profile assuming a spherically symmetric atmosphere (Fjeldbo and Eshleman, 1968; Eshleman, 1973; Sokolovskiy, 2001). The second step is to simulate the spaceborne GNSS RO refractivity retrieval by applying the Abel inversion on the simulated bending angle from step one. In the absence of ducting, the impact parameter increases monotonically with height, allowing a unique solution to the inverse Abel retrieval that is the same as the original refractivity profile input. However, in the presence of an elevated ducting layer, the Abel retrieval systematically underestimates the refractivity profile due to the non-unique Abel inversion problem resulting from the singularity in bending angle across the ducting layer (Sokolovskiy 2003; Xie et al., 2006). It should be noted that after the 100 m vertical smoothing on radiosonde (no smoothing is performed on ERA5) profiles as described in section 2.2, an additional 50 m vertical smoothing has been applied to the simulated bending angle profiles of both radiosonde and ERA5 data sets

8

212   to alleviate the challenge of integration through the very sharp bending angle resulting from

213   ducting in the inverse Abel integration procedure (Feng et al., 2020).

214   Figure 3 shows the end-to-end simulation results for the same radiosonde (a–d) and the colocated

215   ERA5 (e–h) cases from Fig. 2. Figures 3a and 3e show refractivity profiles from the radiosonde

216   (N_{MAGIC}) and the colocated ERA5 (N_{ERA5}) data as well as their corresponding Abel refractivity

217   retrievals (N_{Abel}). The refractivity gradients are shown in Figures 3c and 3g. The derived PBLH is

218   marked by a horizontal dotted line in the refractivity/height space. The peak bending angles in

219   Figures 3d and 3h are consistent with the corresponding sharp refractivity gradient. Figure 3b

220   shows the fractional N-bias between the simulated Abel retrieved RO refractivity profile and the

221   radiosonde, whereas Figure 3f shows the same for the ERA5 profile. Considering the significant

222   spatial and temporal variations of ducting height along the transect, each N-bias profile is displayed

223   as a function of an adjusted height, which is the height minus the corresponding PBLH for the

224   purposes of profile intercomparison. For example, the zero-adjusted height refers to the PBLH for

225   each individual profile. The systematic negative N-bias is shown below the ducting layer marked

226   by the PBLH in both cases, with the biases decreasing at lower altitude, the largest magnitude bias

227   (-5% for radiosonde; -2.5% for ERA5) close to the ducting height and a minimum magnitude

228   approaching zero near the surface.
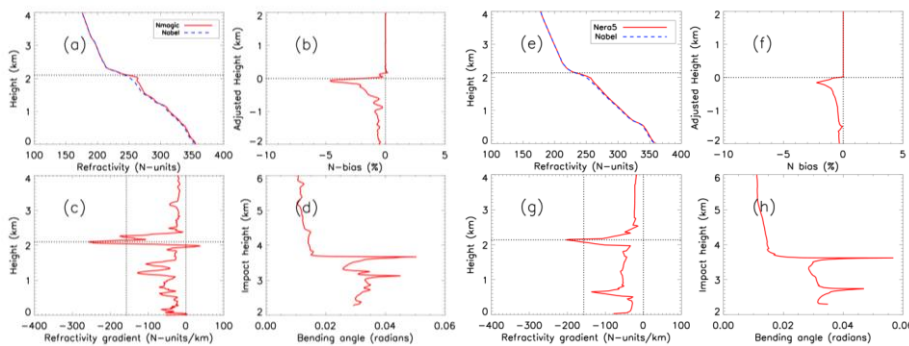
229

230   **Figure 3: End-to-end simulation results for a MAGIC radiosonde launched at 0530 UTC on ~~20121002~~20131002 showing:**
231   **(a) N_{MAGIC} (solid red) and N_{Abel} (blue dashed) from surface to 4 km; (b) PBLH adjusted N-bias; (c) vertical refractivity**
232   **gradient and (d) bending angle vs. impact parameter. Panels e-h show end-to-end simulation results for the colocated ERA5**
233   **profile.**

234   **3   Analysis**

Quality control for radiosonde (and colocated ERA5) profiles was based on five key criteria. First, a total of 19 radiosonde and 24 ERA5 profiles near the southern California coast were removed due to their positions east of −120˚ or anomalously high PBL (PBLH > 3.0 km) with no distinct minimum gradient. The remaining profiles in the easternmost portion of the domain were too few in number to calculate meaningful statistics. Second, any profile lacking critical refraction (i.e. $dN/dz < -157$ N-units km^{-1}) points was excluded from the analysis which resulted in the removal of 47 radiosonde and 176 ERA5 profiles. Third, ~~the~~an anomalously noisy bending angle profile could result in errors in Abel refractivity retrieval and cause positive N-bias. Therefore, the profiles with N-bias greater than +0.5% are excluded resulting in the removal of 61 MAGIC profiles and 16 ERA5 profiles. Fourth, the profiles with only surface ducting, i.e., below 300 m threshold, are discarded. Finally, 25 radiosonde profiles and 2 ERA5 profiles were removed due to the Abel retrieval failure. After implementing all quality control measures, the number of radiosonde and ERA5 profiles used for the N-bias analysis is reduced to 396 and 319 profiles, respectively across the MAGIC transect.

3.1 PBL analysis

To evaluate the ducting properties along the transect from the coast of southern California to Hawaii, we group the MAGIC radiosonde and the colocated ERA5 profiles into eight 5˚ longitude bins between −160.0˚ and −120.0˚, which allows for the assessment of the spatial variation of the PBL, ducting layer, and the associated properties along the transect to be easily illustrated. Figure 4 shows the median value of PBLH (a), minimum gradient (b) and sharpness parameter (c) along the transect. The median-absolute-deviation (MAD) for each parameter is also shown.

In ~~Fig.~~Figure 4a, the MAGIC radiosondes (rds) clearly show ~~the~~a gradual increase of the PBLH along the transect from the shallow stratocumulus-topped PBL (~800 m) near the southern California coast westward to the much deeper trade-cumulus regime (~1.8 km) near Hawaii. A similar structure is seen in the colocated ERA5 data but with an average low bias of 165 m below the radiosonde. ~~However~~Additionally, a nearly 800 m ERA5 underestimation in PBLH over the two westernmost bins near Hawaii is also seen, this is consistent with what is found over the equivalent trade cumulus region of the subtropical southeast Pacific Ocean (Xie et al., 2012). Such a discrepancy could be due to the sensitivity of the gradient method to the vertical resolution of the data. Over the western segment of the transect (near Hawaii), two major gradient layers (one

10

265   at ~1 km and the other at ~2 km) with comparable refractivity gradients are often observed (e.g.,

266   Fig. 2),2) in the ERA5 data. The gradient layer near 2 km is well-known as the trade-wind inversion

267   (Riehl, 1979; Ao et al., 2012; Xie et al., 2012), while the lower-level gradient layer at ~1 km, is

268   generally called a mixing layer (Xie et al., 2006). Due to the differences in vertical sampling noted

269   in Section 2.1, the ERA5 data are more likely to resolve the sharp gradient structure below 1 km

270   than the one at higher altitude. This could result in resolving the mixing layer (below 1 km) with

271   the sharpest refractivity gradient, instead of the trade-wind inversion near 2 km in the ERA5 data.

272   Note that the larger median absolute deviation for the westernmost bins compared to the rest of

273   the transect illustrates the existence of greater PBLH variability closer to the trade-cumulus

274   boundary layer regime. The westward decreasing magnitude of the minimum refractivity gradient

275   (Fig. 4b) and sharpness parameter (Fig. 4c) indicates the westward weakening of moisture lapse

276   rate and/or temperature inversion across the PBL top, which is consistent with the decreasing

277   synoptic-scale subsidence from the California coast to Hawaii (Riehl, 1979).

278
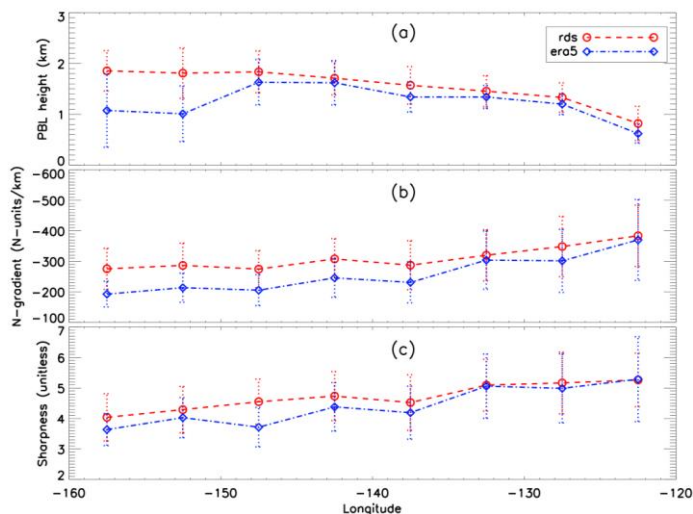
Figure 4: Zonal transect of 5˚ binbinned MAGIC and ERA5 PBLH (a), minimum refractivity gradient and
(b) and sharpness parameter (c) for MAGIC (median in red circle and dashed line, MAD in red dotted error bars) and
ERA5 (median in blue diamond and dot-dashed line, MAD in blue dotted error bars).

282

283   It is also notable that the ERA5 systematically underestimates not only the PBLH but also the

284   magnitude of the minimum gradient across the entire transect. This can also be seen in the

285   sharpness parameter west of −132.5˚. This discrepancy could be partially attributed to the decrease

11

286 in vertical sampling in ERA5 profiles as compared to the radiosondes, the result of which leads to
287 a weaker PBL refractivity gradient and coincides with an increasing PBLH. Therefore, the
288 underestimation of the ERA5 minimum refractivity gradient increases in magnitude from east to
289 west and becomes most prominent near Hawaii where the PBLH reaches the maximum ~~height~~
290 over the region.

291 **3.2 Ducting characteristics**

292 As introduced in Sect. 2.3, the key characteristics of the ducting layer along the transect will be
293 investigated~~, these~~. These characteristics include the ducting layer height, ducting layer thickness
294 (Δh), and ducting strength (ΔN), as well as the average refractivity gradient within the ducting
295 layer ($\Delta N/\Delta h$).
296 The ducting layer heights from both ~~radiosonde~~radiosondes and ERA5 show a westward increase
297 along the transect, as seen in ~~Fig.~~Figure 5a. Note again that the ERA5 shows a systematic ~100–
298 200 m low bias when compared to the radiosondes between −122.5˚ and −147.5˚, with the
299 difference increasing to more than 500 m near Hawaii. The ducting layer thickness is the median
300 height from the bottom of the ducting layer to the top and is expressed in km (Fig. 5b). Ducting
301 thickness (Δh) for MAGIC shows a near constant value of 110 m across the entire transect with
302 only a slight increase to 130 m at −122.5˚, consistent with Ao et al. (2003). Conversely, the ERA5
303 shows a constant but slightly thicker ducting layer to the east of −137.5˚ and then a decreasing
304 thickness to the west of −137.5˚ (Fig. 5b).
305 The ducting layer strength is the decrease in refractivity from the bottom of the ducting layer to
306 the top (Fig. 5c) and the ratio $\Delta N/\Delta h$ reflects the average gradient of the ducting layer (Fig. 5d).
307 The ducting strength (ΔN) for the radiosondes generally ranges from 25 N-units near Hawaii to 40
308 N-units near the coast of California. Both ΔN and $\Delta N/\Delta h$ show an overall westward decreasing
309 trend along the transect which is consistent with the decrease in magnitude of the refractivity
310 gradient (Fig. 4b). Note that MAGIC and ERA5 show similar ducting strength in the eastern part
311 of the region but diverge near −137.5˚ with ERA5 10 to 20 N-units weaker than the MAGIC
312 profiles. On the other hand, ERA5 shows a systematically lower average refractivity gradient
313 ($\Delta N/\Delta h$) than MAGIC throughout the transect, indicating the challenge in ERA5 to consistently
314 resolve the sharp vertical structure in refractivity, and likewise in temperature and moisture

315　profiles, across such a thin ducting layer. The problem becomes acutely clear near the trade

316　cumulus region.
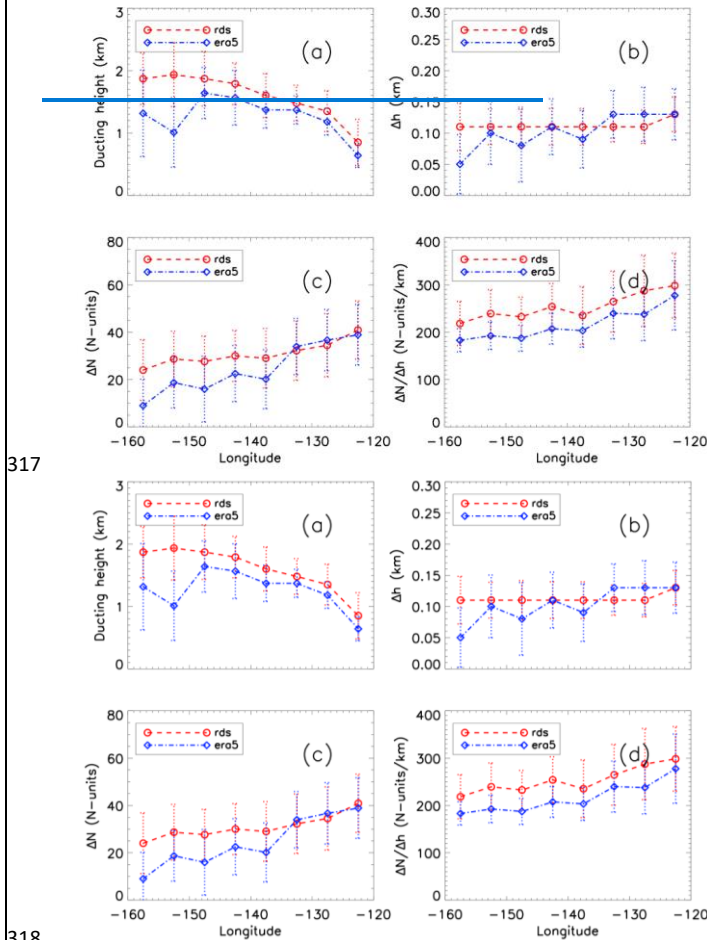
323　Figure 6 shows individual ducting layer ~~thickness~~thicknesses as a function of ducting layer

324　strength~~, with~~. The shape and color of each data point ~~colored by~~is used to identify its respective

325　longitude bin. The relationship between Δh and ΔN is not longitude-dependent for either data set,

326　but a linear trend is evident for thinner ducting layers (Δh < 0.1 km) with weaker ducting strength

Formatted: Font: +Body (Calibri), 11 pt, Not Bold

13

327 ($\Delta N < \sim 25$ N-units). However, for the ducting layers thicker than 0.1 km, such a trend becomes

328 less identifiable, and the ducting strength ΔN begins to show more variability toward larger values.

329

330
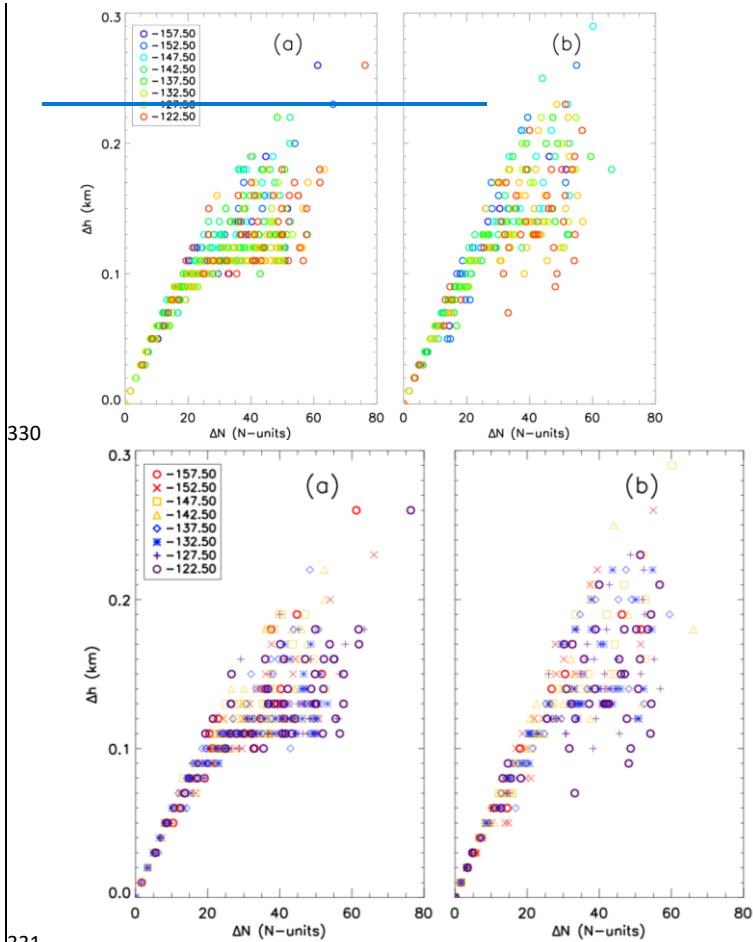
331

332 **Figure 6: Comparison of individual profiles' ducting strength (ΔN) vs. ducting thickness (Δh) for MAGIC (a) and ERA5**

333 **(b). The shape and color of each ~~circle~~character represents the location of the 5° longitude bin of each observation.**

334 **3.3 Ducting-induced GNSS RO N-bias statistics**

335 To estimate the systematic negative N-bias in GNSS RO observations due to ducting, we have

336 applied the end-to-end simulation described in Sect. 2.4 to all radiosonde and ERA5 refractivity

14

337   profiles with at least one elevated ducting layer detected. The *N*-bias along the transect as well as

338   its relationship to the ducting properties are presented below.

3.3.1 Assessing ducting-induced *N*-bias

340   Figure 7 shows a composite of both MAGIC (396 profiles) and ERA5 (319 profiles) *N*-bias profiles

341   which have been displayed as a function of ~~an~~ their zero-adjusted height~~, which is the height minus~~

342   ~~the derived PBLH, with the~~ . The median *N*-bias and MAD ~~overlaid.~~are also shown. The systematic

343   negative *N*-bias peaks at approximately 100 m below the PBLH and decreases at lower

344   ~~altitude~~relative altitudes. The peak median value of the *N*-bias for radiosondes is −5.42% (MAD,

345   2.92%), nearly twice the ERA5 value of −2.96% (MAD, 2.59%), indicating the significant

346   underestimation of ducting strength in ERA5 data. However, the ~~variabilities (~~MAD~~)~~ of the

347   radiosonde and ERA5 data are within 0.33% of each other, indicating that ERA5 data successfully

348   capture the variations of ducting features seen in the radiosondes. It is worth noting that many

349   radiosonde profiles show small negative *N*-biases above the PBLH (i.e., positive zero-adjusted

350   height), which is the result of a secondary ducting layer above the major ducting layer near the

351   PBLH. Few ERA5 profiles show the presence of the secondary ducting layer above PBLH.

352
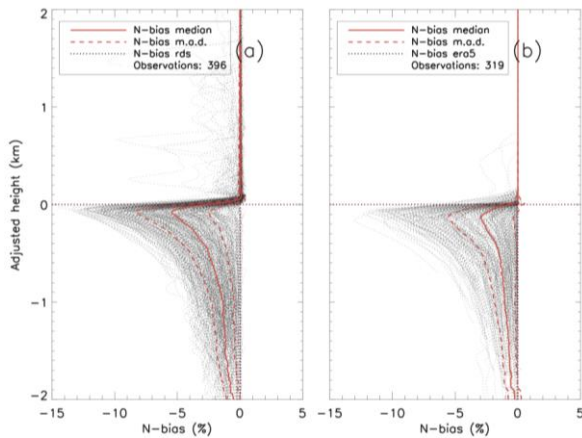
353
354   **Figure 7: Fractional refractivity difference (*N*-bias ~~in %)~~) between the simulated Abel-retrieved refractivity profile and the**
355   **original ~~observation~~observed refractivity profile~~,~~ for all individual observations (dotted gray): (a) MAGIC radiosondes (396**
356   **total profiles) and (b) ERA5 (319 total profiles) with population median (solid red) ± MAD (dashed red). Note the zero value**
357   **in the adjusted height refers to the detected PBLH for each individual *N*-bias profile.**

3.3.2 Zonal variation of the *N*-bias along the transect

To illustrate the large variation in the *N*-bias vertical structure resulting from the spatial variations of ducting height and strength, ~~Fig.~~Figure 8 ~~presents~~shows the median *N*-bias profiles ~~(median ±(±~~ MAD) for each 5˚ bin, replacing the zero adjusted height with the median PBLH for each bin. The zonal radiosonde composite (Fig. 8a) illustrates the westward transition of the median *N*-bias profiles from the largest peak *N*-bias at ~0.8 km near the coast of Los Angeles, California, to a much~~ ~~reduced peak *N*-bias but higher altitude of ~1.8 km at Honolulu, Hawaii. Table 1 lists detailed statistics of the peak *N*-bias values at each bin for both radiosonde and ERA5 data~~.~~ seen in Fig. 8. Although the vertical structure of the *N*-bias profiles along the transect are consistent as seen in Fig. 7, significant changes of the *N*-bias magnitude and its peak height along the transect are seen.

The maximum peak *N*-bias (−7.86%) in the radiosonde data is located at the easternmost of the transect near California (−122.5˚), whereas the minimum peak *N*-bias (−4.37%) is located near the center of the transect (−147.5˚). Similarly, the ERA5 also show the maximum peak *N*-bias (−5.92%) near California (−122.5˚). However, the minimum peak *N*-bias (−0.77%) is found near Hawaii (−157.5˚). Overall, the *N*-bias values for the ERA5 data set are less than the *N*-bias values calculated from the radiosonde data set for ~~ ~~each longitude bin. However, a noticeable difference exists between the ERA5 and radiosonde profiles for the two westernmost longitude bins (−157.5˚ and −152.5˚) where the ERA5 reveals a much lower and weaker *N*-bias than the MAGIC data.

The PBLH is above the height of the peak *N*-bias for both data sets. The MAGIC data ~~shows~~show a maximum difference of 100 m (−~~137~~157.5˚) and a minimum difference of ~~~15~~70 m (−~~152~~142.5˚) while the ERA5 PBLH shows greater values for maximum difference (~~230~~140 m at −~~142~~132.5˚) and ~~ ~~minimum ~~of (45~~difference (60 m at −157.5˚).

381
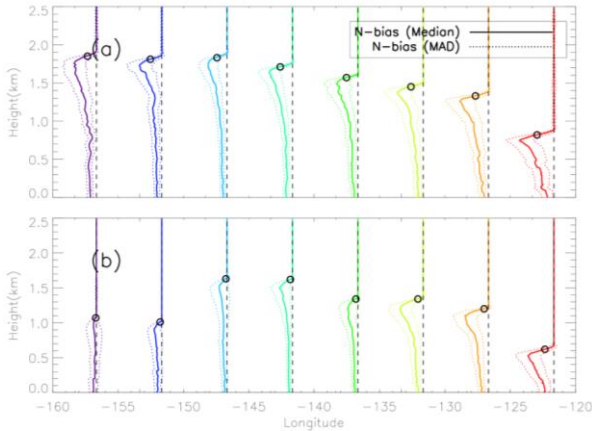
Figure 8: Median *N*-bias (solid) ± MAD (dotted) *N*-bias along the north Pacific transect for MAGIC radiosondes (a) and ERA5 (b). Open circles represent the median PBLH for each 5° bin. Vertical dashed line represents the location of each 5° grid bin. See Table 1 for corresponding values of median and M.A.D. peak *N*-bias.

(margin note)

Formatted: Font: Italic

Table 1: MedianPeak values of median *N*-bias and corresponding MAD peak *N*-bias (%) values for MAGIC radiosondes (RDS) and ERA5 for each 5° bin.

Longitude	Peak N-bias (%)			
	RDS median	RDS MAD	ERA5 median	ERA5 MAD
−157.5°	−5.12	±2.61	−0.77	±1.73
−152.5°	−5.10	±2.97	−1.76	±1.61
−147.5°	−4.37	±2.14	−1.83	±2.10
−142.5°	−5.36	±2.53	−2.95	±2.17
−137.5°	−4.82	±2.96	−2.31	±2.14
−132.5°	−5.90	±3.03	−5.31	±2.68
−127.5°	−6.55	±3.40	−5.45	±2.88
−122.5°	−7.86	±3.15	−5.92	±3.04

Figure 9 further illustrates the peak *N*-bias, median PBL *N*-bias (0.3 km to PBLH), and the near surface *N*-bias (at 0.3 km) at each bin along the transect. Note the median PBL *N*-bias referrefers to the median value from the near-surface (0.3 km) to the PBLH. Contrary to the general trend of westward decrease in magnitude of the minimum refractivity gradient (Fig. 4b) and ducting strength (Fig. 5c), the radiosonde peak *N*-bias shows the maximum (median: −8.10%, MAD: 3.26%) occurs near California (−122.5°) and the minimum (median: −4.85%, MAD: 2.18%) occurs over the transition region (−147.5°) as well as). There is also a slight increase in peak *N*-

17

403   bias to a secondary maximum (median: −6.11%, MAD: 2.85%) near Hawaii (−157.5˚). The

404   median PBL N-bias and the near surface N-bias also show a similar pattern. However, the median

405   N-bias demonstrates a sharp decrease in the eastern half of the domain from −5.25% (MAD:

406   2.71%) at −122.5˚ to −1.71% (MAD: 1.26%) at −137.5˚, and then remains relatively constant over

407   the western half of the domain. Similarly, the near surface N-bias reaches a maximum magnitude

408   of −3.54% (MAD: 2.11%), sharply decreases to −1.06% (MAD: 0.85%) at −137.5˚, and then

409   remains relatively constant over the western half of the domain.

410   Note that normalizing each N-bias profile to the PBLH preserves the magnitude of the N-bias with

411   various heights. Therefore, the relatively large, normalized N-biases observed near Hawaii

412   indicates more persistent ducting over the trade-cumulus boundary layer regime compared to the

413   transition region in the middle of the transect at -147.5˚ (Fig. 8a).

414   On the other hand, the ERA5 data show a westward decrease of all three N-biases, systematically

415   underestimating all three as compared to the radiosondes. This is expected as the decrease of ERA5

416   vertical resolution at higher altitude leads to a weaker PBL N-gradient observation (Fig. 4b), and

417   thus weaker ducting and a smaller ducting-induced N-bias. Such underestimation of the N-bias in

418   the ERA5 reanalysis minimizes near California where the PBLH is lowest but becomes more

419   severe westward with an increase in height, reaching a maximum magnitude N-bias difference

420   near Hawaii. In this case, the peak N-bias is merely −0.71% (MAD: 1.80%) as compared to −6.23%

421   (MAD: 2.98%) at −122.5˚ (Fig. 9a). The large difference seen in the N-bias along the transect

422   strongly indicates the challenges of the ERA5 data to resolve the sharp gradient across the ducting

423   layer, resulting in a large variation in PBLH of the ERA5 data in the western segment of the region.

424   The increasing difference between the radiosonde and ERA5 data from east to west is most

425   pronounced in the peak N-bias cross-section (Fig. 9a) but is also evident in both the median N-bias

426   (Fig. 9b) as well as the near surface N-bias (Fig. 9c).
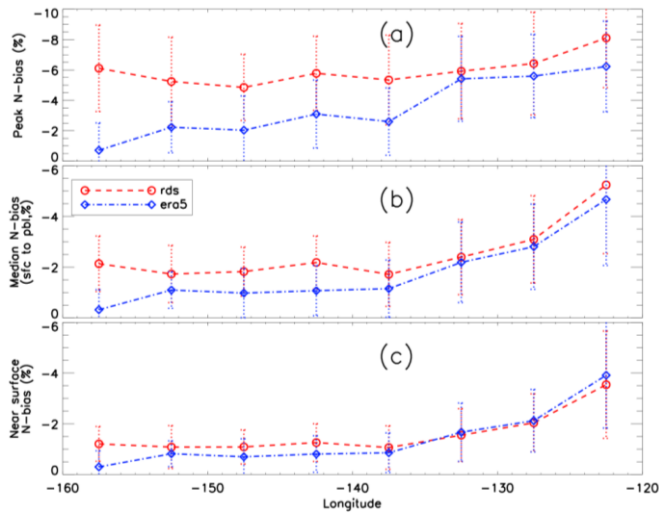
Figure 9: Zonal transect of 5° ~~bin~~binned (a) peak *N*-bias, (b) median PBL *N*-bias (0.3 km to PBLH), and (c) near surface *N*-bias at 0.3 km for MAGIC (median in red circle and red-dashed line, MAD in red-dotted error bar) and ERA5 (median in blue diamond and dot-dashed line, MAD in blue-dotted error bar)

4   Summary and Conclusions

In this study, radiosonde profiles from the MAGIC field campaign have been analyzed to investigate ducting characteristics and the induced systematic refractivity biases in GNSS RO retrievals over the Northeastern Pacific Ocean between Hawaii and California. Colocated ERA5 model reanalysis data were used as a secondary comparison to the radiosonde observations.

The nearly 1-year high-resolution MAGIC radiosonde data set reveals the frequent presence of ducting marked by a sharp refractivity gradient resulting from the large moisture lapse rate across a strong temperature inversion layer. The PBLH increases by more than 1 km along the transect from California to Hawaii, while the magnitude of the refractivity gradient decreases by 100 N-units km^{-1}. The zonal gradient of both variables illustrates the transition of the PBL from shallow stratocumulus adjacent to the California coast to deeper trade-wind cumulus that are prevalent near the Hawaiian Islands.

End-to-end ~~simulation~~simulations on all radiosonde and ERA5 refractivity profiles ~~has~~have been conducted to estimate the systematic negative *N*-bias in GNSS RO observations. The ducting layer maintains remarkably consistent thickness (~110 m) along the transect with westward decreasing strength and increasing height. The ERA5 slightly underestimates both the height and strength of

19

the ducting layer as well as the PBLH. A systematic negative N-bias below the ducting layer is observed throughout the transect, peaking (−5.42%) ~~approximately 80 meters~~slightly below the PBLH, and gradually decreasing towards the surface (−0.5%).

MAGIC radiosondes indicate larger values of both ducting strength (ΔN) and thickness (Δh) than ERA5 in the western half of the transect. The opposite is true in the eastern portion of the domain~~,~~ and is likely associated with the transition of the cloud layer from open-cell cumulus in the west to stratocumulus and stratus in the east (Wood et al., 2011; Bretherton et al., 2019). ERA5 systematically underestimates the average ducting layer gradient ($\Delta N/\Delta h$) comparing to the radiosondes. The largest N-bias is found over the region with strongest ducting and largest sharpness parameter. It is worth noting that the PBL over the western portion of the transect near Hawaii frequently shows two major gradient layers (a mixing layer at ~1 km and the trade-inversion at ~2 km), with comparable N-gradients (e.g., Fig. 2). The much lower PBLH seen in ERA5 in this region is likely due, in part, to the decreasing number of model levels in ERA5 at higher altitude, which could lead to a higher possibility of identifying the lower gradient layer as the PBLH. However, the impact of the vertical resolution and on the performance of the gradient method for PBLH detection has not been performed in this study ~~and warrants~~. Further, the ERA5 results may be affected by the interpolation resolution and gradient are calculation. Both warrant a more comprehensive study in the future.

5   Data availability

Data for the Marine Atmospheric Radiation Measurement (ARM) GCSS Pacific Cross Section Intercomparison (GPCI) Investigation of Clouds (MAGIC, Zhou et al., 2015) can be accessed through the U.S. Department of Energy's Office of Science https://www.arm.gov/research/campaigns/amf2012magic.

Data for the ECMWF Reanalysis version 5 (ERA5, Hersbach et al., 2020) can be accessed at https://www.ecmwf.int/en/forecasts/dataset/ecmwf-reanalysis-v5.

6   Author contribution

Author Thomas Winning is responsible for all original text ~~and,~~ data analysis, and production of graphics. Author Kevin Nelson contributed by providing updated data processing and end-to-end

simulation code, colocation of ERA5 data with MAGIC observations, and ~~first and second round~~manuscript edits. Author Feiqin Xie is the academic advisor for the primary author and also provided draft edits and paper organization and writing guidance.

7 Competing interests

The authors declare no competing interests, see Acknowledgements for current affiliations.

References

Anthes, R. A., and Coauthors: The COSMIC/FORMOSAT-3 Mission: Early Results, BAMS, 89, 313–334, doi.org/10.1175/bams-89-3-313, 2008.

Ao, C. O., Meehan T. K., Hajj, G. A., Mannucci, A. J., and Beyerle, G.: Lower Troposphere Refractivity Bias in GPS Occultation Retrievals, J. Geophys. Res., 108, 4577, doi:10.1029/2002JD003216, 2003.

Ao, C. O.: Effect of Ducting on Radio Occultation Measurements: An Assessment Based on High-resolution Radiosonde Soundings, Radio Sci., 42, RS2008, doi.org/10.1029/2006RS003485, 2007.

505

506 Ao, C. O., Chan, T. K., Iijima, A., Li, J.-L., Mannucci, A. J., Teixeira, J., Tian, B., and Waliser, D. E.: Planetary
507 Boundary Layer Information from GPS Radio Occultation Measurements, in: Proceedings of the GRAS SAF
508 Workshop on Applications of GPSRO Measurements, Vol. 5 of, GRAS SAF Workshop on Applications of GPSRO
509 Measurements, Reading, United Kingdom, ECMWF and EUMETSAT, 123–131,
510 https://www.ecmwf.int/sites/default/files/elibrary/2008/7459-planetary-boundary-layer-information-gps-radio-
511 occultation-measurements.pdf, 16–18 June, 2008.

512

513 Ao, C. O., Waliser, D. E., Chan, S. K., Li, J.-L., Tian, B., Xie, F., and Mannucci, A. J.: Planetary boundary layer
514 heights from GPS radio occultation refractivity and humidity profiles, J. Geophys. Res., 117, D16117,
515 doi:10.1029/2012JD017598, 2012.

516

517 Basha, G., and Ratnam, M. V.: Identification of atmospheric boundary layer height over a tropical station using high-
518 resolution radiosonde refractivity profiles: Comparison with GPS radio occultation measurements, J. Geophys. Res.,
519 114, doi.org/10.1029/2008jd011692, 2009.

520

521 Beyerle, G., Gorbunov, M. E., and Ao, C.O.: Simulation studies of GPS radio occultation measurements, Radio Sci.,
522 38, 1084, doi:10.1029/2002RS002800, 2003.

523

524 Bretherton, C.S., and Coauthors: Cloud, Aerosol, and Boundary Layer Structure across the Northeast Pacific
525 Stratocumulus–Cumulus Transition as Observed during CSET, Mon.Wea. Rev., 147, 2083–2102. DOI:
526 10.1175/MWR-D-18-0281, 2019

527

528 Eshleman, V.R.: The radio occultation method for the study of planetary atmospheres, Planet. Space Sci., 21, 1521-
529 1531, doi.org/10.1016/0032-0633(73)90059-7, 1973.

530

531 Feng, X., Xie, F., Ao, C.O., and Anthes, R.A.: Ducting and Biases of GPS Radio Occultation Bending Angle and
532 Refractivity in the Moist Lower Troposphere, J. Atmos. Oceanic Technol., 37, 1013–1025, doi.org/10.1175/JTECH-
533 D-19-0206.1, 2020.

534

535 Fjeldbo, G., and Eshleman, V.R.: The Atmosphere of Mars Analyzed by Integral Inversion of the Mariner IV
536 Occultation Data, Planet. Space Sci., 16, 1035-1059, doi.org/10.1016/0032-0633(68)90020-2, 1968.

537

538 Fjeldbo, G., Kliore, A.J., and Eshleman, V.R.: The Neutral Atmosphere of Venus as Studied with the Mariner V Radio
539 Occultation Experiment, Astron. J., 76, 123-140, doi.org/10.1086/111096, 1971.

540

541 Garratt, J. R.: Review: the atmospheric boundary layer, Earth-Sci. Rev., 37, 89–134, 1994

542

543 Guo, P., Kuo, Y. H., Sokolovskiy, S. V., and Lenschow, D. H.: Estimating Atmospheric Boundary Layer Depth Using

544 COSMIC Radio Occultation Data, J. Atmos. Sci., 68, 1703–1713, doi.org/10.1175/2011jas3612.1, 2011.

545

546 Gorbunov, M. E.: Canonical transform method for processing radio occultation data in the lower troposphere, Radio

547 Sci., 37(5), 1076, doi:10.1029/2000RS002592, 2002.

548
549 Gorbunov, M. E., Benzon, H. H., Jensen, A.S, Lohmann, M.S., and Nielsen, A.S.: Comparative analysis of radio

550 occultation processing approaches based on Fourier integral operators. Radio Sci., 39, RS6004,

551 https://doi.org/10.1029/2003RS002916, 2004

552

553 Healy, S. B.: Radio occultation bending angle and impact parameter errors caused by horizontal refractive index

554 gradients in the troposphere: A simulation study, J. Geophys. Res, 106, D11, 11875–11889,

555 doi:10.1029/2001JD900050, 2001.

556

557 Hersbach, H., Bell, B., Berrisford, P., Hirahara, S., Horányi, A., Muñoz-Sabater, J., Nicolas, J., Peubey, C., Radu, R.,

558 Schepers, D., Simmons, A., Soci, C., Abdalla, S., Abellan, X., Balsamo, G., Bechtold, P., Biavati, G., Bidlot, J.,

559 Bonavita, M., De Chiara, G., Dahlgren, P., Dee, D., Diamantakis, M., Dragani, R., Flemming, J., Forbes, R., Fuentes,

560 M., Geer, A., Haimberger, L., Healy, S., Hogan, R. J., Hólm, E., Janisková, M., Keeley, S.,

561 Laloyaux, P., Lopez, P., Lupu, C., Radnoti, G., de Rosnay, P., Rozum, I., Vamborg, F., Villaume, S., and Thépaut, J.-

562 N.: The ERA5 Global Reanalysis, Q. J. Roy. Meteor. Soc., 146, 1999–2049, https://doi.org/10.1002/qj.3803, 2020.

563
564 Ho, S.-P., Peng, L., Anthes, R. A., Kuo, Y.-H., and Lin, H.-C.: Marine boundary layer heights and their longitudinal,

565 diurnal and inter-seasonal variability in the southeast Pacific using COSMIC, CALIOP, and radiosonde data. J.

566 Climate, 28, 2856–2872, https://doi.org/10.1175/JCLI-D-14-00238.1, 2015.

567
568 Jensen, A. S., Lohmann, M.S., Nielsen, A.S. and Benzon, H.-H.: Geometrical optics phase matching of radio

569 occultation signals, Radio Sci., 39, RS3009, doi:10.1029/2003RS002899, 2004.

570

571 Jensen, A. S., Lohmann, M.S., Benzon, H.-H, and Nielsen, A.S.: Full spectrum inversion of radio occultation signals,

572 Radio Sci., 38(3), 1040, doi:10.1029/2002RS002763, 2003.

573

574 Johnston, B. R., Xie, F., and Liu, C.: The effects of deep convection on regional temperature structure in the tropical

575 upper troposphere and lower stratosphere, J. Geophys. Res.: Atmos., 123, 1585−1603,

576 doi.org/10.1002/2017JD027120, 2018.

577

578 Klein, S. A., and Hartmann, D. L.: The seasonal cycle of low stratiform clouds. Journal of Climate, 6, 1587−1606,

579 doi:10.1175/1520-0442(1993)006<1587:TSCOLS>2.0.CO;2, 1993.

580

581 Kursinski, E. R., Hajj, G. A., Schofield, J. T., Linfield, R. P., and Hardy, K. R.: Observing Earth's atmosphere with
582 radio occultation measurements using the Global Positioning System, J. Geophys. Res.: Atmos., 102, 23429−23465,
583 doi.org/10.1029/97jd01569, 1997.

584

585 Kursinski, E. R., G. A. Hajj, Leroy, S. S., and Herman, B.: The GPS Radio Occultation Technique. Terr. Atmos.
586 Ocean. Sci. (TAO), 11, 53−114, 2000.

587

588 Lewis, E. R.: Marine ARM GPCI Investigation of Clouds (MAGIC) Field Campaign Report. U.S. Department of
589 Energy, https://doi.org/10.2172/1343577, 2016.

590

591 Maddy, E. S. and Barnet, C. D.: Vertical resolution estimates in version 5 of AIRS operational retrievals. IEEE
592 Transactions on Geoscience and Remote Sensing, 46, 2375−2384, doi:10.1109/TGRS.2008.917498, 2008.

593

594 Nelson, K. J., Xie, F., Ao, C. O., and Oyola-Merced, M. I.: Diurnal Variation of the Planetary Boundary Layer Height
595 Observed from GNSS Radio Occultation and Radiosonde Soundings over the Southern Great Plains. J. Atmos.
596 Oceanic Tech., 38, 2081−2093, https://doi.org/10.1175/jtech-d-20-0196.1, 2021.

597

598 Nelson, K. J., Xie, F., Chan, B. C., Goel, A., Kosh, J., Reid, T. G. R., Snyder, C. R., and Tarantino, P. M.: GNSS
599 Radio Occultation Soundings from Commercial Off-the-Shelf Receivers Onboard Balloon Platforms, Atmos. Meas.
600 Tech., https://doi.org/10.5194/amt-2022-198, 2022.

601

602 Painemal, D., Minnis, P., and Nordeen, M.: Aerosol variability, synoptic-scale processes, and their link to the cloud
603 microphysics over the northeast Pacific during MAGIC, J. Geophys. Res. Atmos., 120, 5122–5139,
604 doi:10.1002/2015JD023175, 2015.

605

606 Patterson, W. L.: Climatology of Marine Atmospheric Refractive Effects: A Compendium of the Integrated Refractive
607 Effects Prediction System (IREPS) Historical Summaries. Naval Ocean Systems Center,
608 https://apps.dtic.mil/sti/pdfs/ADA155241.pdf, 1982.

609

610 Ramanathan, V., Cess, R. D., Harrison, E. F., Minnis, P., Barkstrom, B. R., Ahmad, E., and Hartmann, D.: Cloud-
611 radiative forcing and climate: Results from the Earth Radiation Budget Experiment, Science, 243, 57–63,
612 DOI:10.1126/science.243.4887.57, 1989.

613

614 Riehl, H.: Climate and weather in the tropics. London: Academic Press. 611 pp. ISBN 0.12.588180.0

615

616 Rocken, C., Anthes, R., Exner, M., Hunt, D., Sokolovskiy, S., Ware, R., Gorbunov, M., Schreiner, W., Feng
617 D., Herman B., Kuo, Y.-H., Zou, X.: Analysis and validation of GPS/MET data in the neutral atmosphere. J. Geophys.
618 Res., 102, 29849−29866, https://doi.org/10.1029/97JD02400, 1997.

620 Schreiner, W. S., Weiss, J.P., Anthes, R.A., Braun, J., Chu, V., Fong, J., Hunt, D., Kuo, Y.-H., Meehan, T., Serafino,
621 W., Sjoberg, J., Sokolovskiy, C., Talaat, E., Wee, T.K., Zeng, Z.: COSMIC-2 Radio Occultation Constellation: First
622 Results. Geophys. Res. Lett., 47, https://doi.org/10.1029/2019gl086841, 2020.

624 Seidel, D. J., Ao, C.O. and Li, K.: Estimating climatological planetary boundary layer heights from radiosonde
625 observations: Comparison of methods and uncertainty analysis, J. Geophys. Res., 115, D16114,
626 doi:10.1029/2009JD013680, 2010.

628 Smith, E. K. and Weintraub, S.: The Constants in the Equation for Atmospheric Refractivity Index at Radio
629 Frequencies. Proc. IRE, 41, 1035−1037, doi:10.1109/JRPROC.1953.274297, 1953.

631 Sokolovskiy, S. V.: Modeling and Inverting Radio Occultation Signals in the Moist Troposphere. Radio Sci., 36,
632 441−458, https://doi.org/10.1029/1999RS002273, 2001.

634 Sokolovskiy, S. V.: Effect of super refraction on inversions of radio occultation signals in the lower troposphere.
635 Radio Sci., 38 (3), https://doi.org/10.1029/2002RS002728, 2003.

637 Sokolovskiy, S. V., Kuo, Y.-H., Rocken, C., Schreiner, W. S., Hunt, D. and Anthes, R. A., 2006: Monitoring the
638 atmospheric boundary layer by GPS radio occultation signals recorded in the open-loop mode. Geophys. Res. Lett.,
639 33, L12813, doi:10.1029/2006GL025955, 2006.

641 Stull, R., Santoso, E., Berg, L. K., and Hacker, J.: Boundary Layer Experiment 1996 (BLX96), BAMS, 78,
642 1149−1158, doi: 10.1175/1520-0477(1997)078<1149:BLEB>2.0.CO;2, 1997.

644 Stull, R. B.: An Introduction to Boundary Layer Meteorology. Kluwer Academic Publishers, 666 pp., ISBN 90-277-
645 2768-6, 1988.

647 von Engeln, A. and Teixeira, J.: A Planetary Boundary Layer Height Climatology Derived from ECMWF Reanalysis
648 Data, J. Climate, 26, 6575−6590, https://doi.org/10.1175/jcli-d-12-00385.1, 2013.

650 Winning, T. E., Chen, Y.-L., and Xie, F.: Estimation of the marine boundary layer height over the central North Pacific
651 using GPS radio occultation, Atmospheric Research, 183, 362−370, https://doi.org/10.1016/j.atmosres.2016.08.005,
652 2017.

653

654 Wood, R., Mechoso, C. R., Bretherton, C. S., Weller, R. A., Huebert, B., Straneo, F., Albrecht, B. A., Coe, H., Allen,

655 G., Vaughan, G., Daum, P., Fairall, C., Chand, D., Gallardo Klenner, L., Garreaud, R., Grados, C., Covert, D. S.,

656 Bates, T. S., Krejci, R., Russell, L. M., de Szoeke, S., Brewer, A., Yuter, S. E., Springston, S. R., Chaigneau, A.,

657 Toniazzo, T., Minnis, P., Palikonda, R., Abel, S. J., Brown, W. O. J., Williams, S., Fochesatto, J., Brioude, J., and

658 Bower, K. N.: The VAMOS Ocean-Cloud-Atmosphere-Land Study Regional Experiment (VOCALS-REx): goals,

659 platforms, and field operations, Atmos. Chem. Phys., 11, 627−654, https://doi.org/10.5194/acp-11-627-2011, 2011.

660

661 Xie, F., Syndergaard, S., Kursinski, E. R., and Herman, B.M.: An Approach for Retrieving Marine Boundary Layer

662 Refractivity from GPS Occultation Data in the Presence of Super-refraction. J. Atmos. Oceanic Technol., 23,

663 1629−1644, https://doi.org/10.1175/JTECH1996.1, 2006.

664

665 Xie, F., Haase, J. S., and Syndergaard, S.: Profiling the Atmosphere Using the Airborne GPS Radio Occultation

666 Technique: A Sensitivity Study. IEEE Transactions on Geoscience and Remote Sensing, 46, 3424−3435,

667 https://doi.org/10.1109/tgrs.2008.2004713, 2008.

668

669 Xie, F., Wu, D. L., Ao, C. O., Kursinski, E. R., Mannucci, A. J., and Syndergaard, S.: Super-refraction effects on GPS

670 radio occultation refractivity in marine boundary layers, Geophys. Res. Lett., 37,

671 https://doi.org/10.1029/2010gl043299, 2010.

672

673 Xie, F., Wu, D. L., Ao, C. O., Mannucci, A. J., and Kursinski, E. R.: Advances and limitations of atmospheric boundary

674 layer observations with GPS occultation over southeast Pacific Ocean, Atmos. Chem. Phys., 12, 903−918,

675 doi:10.5194/acp-12-903-2012, 2012.

676

677 Zhou, X., Kollias, P., and Lewis, E.: Clouds, precipitation and marine boundary layer structure during MAGIC. J.

678 Climate, 28, 2420−2442, https://doi.org/10.1175/JCLI-D-14-00320.1, 2015.